On the modulation of a plane wave to oblique perturbations in finite water depth

Jiacheng Yang[1*] , Jinyu Yao[1] and Xinshu Zhang[1†]

[1]State Key Laboratory of Ocean Engineering, Shanghai Jiao Tong University, Shanghai 200240, China

Highlights

- The instability regions are re-drawn by ZE with kernels in a Hamiltonian form.
- The growth rates in arbitrary water depth by the HOS method and the discretized form of ZE are summarized and the results agree well with each other in particular for the most unstable modes.
- There is a reduction of modulational instability with decreasing the depth and there is still modulational instability in terms of $k_0h = 0.8$, which leads to a strong amplitude growth.

1   Introduction

For two-dimensional modulational instability, a carrier wave can be perturbated with a pair of collinear sidebands and the water depth plays an essential role. There is an evident threshold of the dimensionless water depth $k_0h = 1.363$ (k_0 is the wavenumber of the carrier wave and h is the water depth), which was first found by Benjamin (1967) and Whitham (1967), and confirmed by Janssen & Onorato (2007). As the result of the finite water depth, the wave-induced current and mean surface elevation are generated, which weakens the modulational instability and makes less focusing of the wave energy. Further more, it disappears when $k_0h < 1.363$ and hence the uniform wave train is stable.

However, for three-dimensional cases, a carrier wave is perturbated by a pair of oblique sidebands. Different from the former, the modulational instability can be triggered even when $k_0h < 1.363$. Benney & Roskes (1969) indicated that the unstable regions are limited in a narrow and approximately straight domain in any water depth except $k_0h = 0.38$ where the domain reduces to a straight line. In addition, by using an integro-differential equation of Zakharov (1968), Crawford *et al.* (1981) obtained the horn shape unstable region in the condition of infinite water depth. Stiassnie & Shemer (1984) further studied the same topic with the same approach but in finite water depth and the instability domain. The maximum growth rates were compared with those in McLean (1982). The experiment by Toffoli *et al.* (2013) and the numerical simulations by Fernandez *et al.* (2014) also confirmed the same conclusion and indicated that the modulational instability cannot sustain a substantial amplitude growth for the relative water depth $k_0h < 0.8$. The selected sideband is located at the angle of about 35° on the wavenumber plane, which is based on the nonlinear Schrödinger equation. The experimental results also showed a larger limiting k_0h because a dissipative process is involved inevitably.

In the present study, combined with theoretical analyses by the Zakharov integro-differential equation, direct numerical simulations of the Euler equations are performed using a higher-order spectral method to investigate the modulational instability in finite water depth, in particular for oblique sidebands. The instability regions are also re-drawn by the Zakharov equation with kernels in a Hamiltonian form. Another objective is to find out the threshold water depth where the modulational instability diminishes for oblique cases within the scope of the Zakharov equation.

2   Theoretical Model

The Benjamin-Feir instability of Stokes waves can be considered as a special quartet or a degenerate case of the four-wave resonant. The carrier wave is counted twice and satisfies $\boldsymbol{k_1} = \boldsymbol{k_2} = (k_0, 0)$. The two sidebands $\boldsymbol{k_3} = \boldsymbol{k_1} + (K_x, K_y)$ and $\boldsymbol{k_4} = \boldsymbol{k_1} - (K_x, K_y)$ whose phases are shifted by $-\pi/4$ satisfy

$$2\boldsymbol{k_1} = \boldsymbol{k_3} + \boldsymbol{k_4}, \ |2\omega_1 - \omega_3 - \omega_4| < O(\epsilon^2), \tag{1}$$

where ϵ is the wave steepness, $\boldsymbol{k_j}$ are the wavenumbers and ω_j are the angular frequencies.

According to Crawford *et al.* (1981), Stiassnie & Shemer (1984) and Mei *et al.* (2005), the theoretic analyses are started by the discretized differential equations based on the well-known Zakharov equation (ZE),

$$i\frac{dB_1}{dt} = (T_{1111}|B_1|^2 + 2T_{1313}|B_3|^2 + 2T_{1414}|B_4|^2)B_1 + 2T_{1134}e^{i\Delta_{1134}t}B_1^*B_3B_4, \tag{2}$$

$$i\frac{dB_3}{dt} = (2T_{3131}|B_1|^2 + T_{3333}|B_3|^2 + 2T_{3434}|B_4|^2)B_3 + T_{3411}e^{-i\Delta_{1134}t}B_1^2B_4^*, \tag{3}$$

$$i\frac{dB_4}{dt} = (2T_{4141}|B_1|^2 + 2T_{4343}|B_3|^2 + T_{4444}|B_4|^2)B_4 + T_{4311}e^{-i\Delta_{1134}t}B_1^2B_3^*, \tag{4}$$

---

*Presenting author

†xinshuz@sjtu.edu.cn

where B_j are the wave action amplitudes and T with different subscripts are the interaction kernels of ZE.

As only the short-time solution of the equation is concerned, it is reasonable to take the assumption that the initial amplitudes of two sidebands are far less than that of the carrier wave (i.e., $|B_3|, |B_4| \ll |B_1|$). The solutions to the equations linearized through the zeroth order and the first order can be obtained as

$$B_1 = \beta_1 e^{-iT_{1111}|\beta_1|^2 t}, \ \beta_1 = B_1(0), \tag{5}$$

$$B_3 = \beta_3 e^{-i(\frac{1}{2}\Delta_{1134}+T_{1111}|\beta_1|^2+\sigma)t}, \ \beta_3 = B_3(0), \tag{6}$$

$$B_4 = \beta_4 e^{-i(\frac{1}{2}\Delta_{1134}+T_{1111}|\beta_1|^2-\sigma^*)t}, \ \beta_4 = B_4(0), \tag{7}$$

where the relation between the wave amplitude a_j and the wave action amplitude B_j satisfies $a_j = \frac{1}{\pi}\sqrt{\frac{\omega_j}{2g}}|B_j|$ and $\Delta_{1134} = 2\omega_1 - \omega_3 - \omega_4$ is the detuning factor.

The eigenvalue σ is given as $\sigma = (T_{3131} - T_{4141})\beta_1^2 \pm \sqrt{D}$ with

$$D = \left[\frac{1}{2}\Delta_{1134} + (T_{1111} - T_{3131} - T_{4141})\beta_1^2\right]^2 - T_{3411}T_{4311}\beta_1^4, \tag{8}$$

which is the essential criterion of modulation instability. If the value of D is positive, the wave train will be stable and B_3 and B_4 will maintain the initial values. On the contrary, the growth rate is defined as the imaginary part of σ, i.e., Im $\sigma = \sqrt{-D}$ when D is negative, and B_3 and B_4 will increase exponentially over time. Thus the growth rates in finite depth are able to form complete characterization.

A limitation for the application of ZE in finite depth is that the kernels with the form of T_{1111} and T_{1212} are non-unique. Fortunately, the former one has been resolved by Stiassnie & Shemer (1984) and Janssen & Onorato (2007) and the expression of the latter one is given by Stiassnie & Gramstad (2009). The kernels we use in the present work are consistent with those by Janssen & Onorato (2007) and Janssen (2009), which are slightly different from those by Stiassnie & Shemer (1984) and Stiassnie & Gramstad (2009). And the two expressions are identical under the condition of the exact four-wave resonant.

Another limitation is that for stationary wave steepness, ZE is not suitable for the particularly small water depth, in which there will be an abnormal increase for the growth rate. Zakharov (1999) discussed that the weakly-nonlinear theory has narrow frames of applicability in shallow water.

3 Direct Numerical Simulations

The numerical model with a higher-order spectral (HOS, Dommermuth & Yue (1987), West et al. (1987)) method is applied to validate the predictions of growth rate. According to the potential flow theory, the velocity potential $\phi(\boldsymbol{x}, z, t)$ in the fluid domain satisfies the Laplace equation $\nabla_{\boldsymbol{x}}^2 \phi + \phi_{zz} = 0$. The nonlinear kinematic and dynamic surface boundary conditions are rewritten as

$$\frac{\partial \eta}{\partial t} = \left(1 + |\nabla_{\boldsymbol{x}}\eta|^2\right)W - \nabla_{\boldsymbol{x}}\phi^S \cdot \nabla_{\boldsymbol{x}}\eta, \ \text{at } z = \eta(\boldsymbol{x}, t), \tag{9}$$

$$\frac{\partial \phi^S}{\partial t} = -g\eta - \frac{1}{2}|\nabla_{\boldsymbol{x}}\phi^S|^2 + \frac{1}{2}\left(1 + |\nabla_{\boldsymbol{x}}\eta|^2\right)W^2, \ \text{at } z = \eta(\boldsymbol{x}, t), \tag{10}$$

where $\nabla_{\boldsymbol{x}}$ is the horizontal gradient operator, $\phi^S(\boldsymbol{x}, t) = \phi(\boldsymbol{x}, z = \eta(\boldsymbol{x}, t), t)$ is the velocity potential of the free surface, and $W(\boldsymbol{x}, t) = \phi_z|_{z=\eta}$ is the vertical velocity at the free surface. In addition, we assume a constant water depth h and the vertical velocity at the bottom is zero, that is, $\phi_z|_{z=-h} = 0$.

The HOS method is a Fourier spectral collocation method (also called a pseudo-spectral method), by which $\nabla_{\boldsymbol{x}}\eta$ and $\nabla_{\boldsymbol{x}}\phi^S$ are able to be solved. As for W, a series of expansions in wave steepness ϵ is performed up to the HOS order $M = 3$, which is chosen to capture the third-order non-linearity in the modulational instability. In addition, a 4th-order Runge–Kutta time integration with $\Delta t = T_1/32$ is applied and there is no relaxation period because the nonlinear initial conditions for the elevation and the velocity potential are applied. The code for the HOS method is developed in house and a GPU acceleration algorithm is adopted to make it more efficient (see Liu & Zhang (2019)).

In this study, we consider a square computational domain with periodic boundary conditions of $L_x \times L_y = 50\lambda_1 \times 50\lambda_1$ (λ_1 is the wavelength corresponding to $\boldsymbol{k_1}$) with $N_x \times N_y = 1024 \times 1024$ to ensure enough nodes in one wavelength and $\boldsymbol{k_1} = (1, 0)$ m^{-1} with $\lambda_1 = 6.28$ m. Thus, the wavenumber resolution is d$k_x = $ d$k_y = 0.02$ m^{-1}, which allows us to accurately extract the changes of the carrier wave and sidebands. The initial surface and velocity potential are obtained by superimposing the carrier wave $(k_0, 0)$ which propagates along the x direction and two sidebands $(k_0 + K_x, K_y)$ and $(k_0 - K_x, -K_y)$. The amplitudes of perturbations are only one percent of the carrier-wave amplitude which is denoted by a_0 for a long steady increase.

4 Results

As results of Eq. (8) with the kernels by Janssen & Onorato (2007) and Janssen (2009), the unstable regions of modulational instability from $k_0h = 0.8$ to $k_0h = 1.78$ and $k_0h = 100$ (i.e., infinite water depth) are shown by contour maps in Fig. 1 with the typical dimensionless wave steepness $k_0a_0 = 0.10$. The maximum growth rate is marked by $\Diamond$. The threshold of the dimensionless water depth $k_0h = 1.363$ can be clearly detected and the

values on the x-axis become zero when $k_0 h < 1.363$. As for three-dimensional cases, the unstable regions are distributed in a relatively wide horn-like domain for $k_0 h > 1.363$ and along a narrow arc for $k_0 h < 1.363$. It is worth noting that the second unstable region appears for $k_0 h < 1.0$, which is located at $K_x/k_0 > 0.8$. It is also reported by Stiassnie & Shemer (1984) and Gramstad & Trulsen (2011). This paper concentrates on the main unstable region and the cases of the second unstable region are not included.

The cases for direct numerical simulations by the HOS method are marked in the Fig. 1 with △ and also listed in the Tab. 1. These are the sidebands with the largest growth rate under the corresponding water depth at relatively lower but reasonable resolution. It is caused by the limitation of the resolution of computational domain and only the sidebands matching the resolution are selected for the convenience of wavenumber spectrum analysis. Nevertheless, without loss of generality, the growth rates of the sidebands △ for the actual calculation are almost the same as the prediction ◇ by ZE although the locations are slightly different from each other.
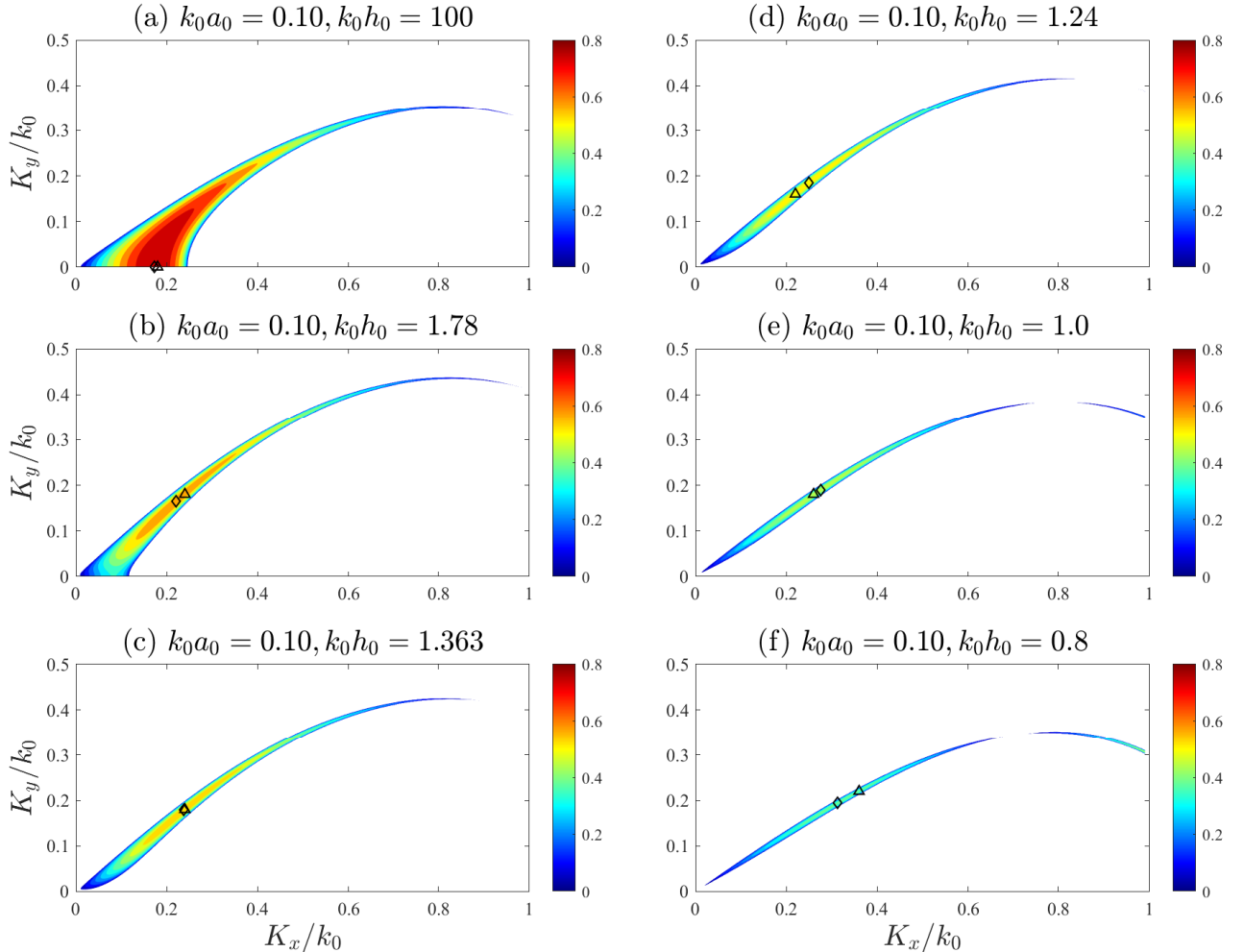
Figure 1: The non-dimensional growth rate G' in different water depths for $k_0 a_0 = 0.10$.

The detailed results are summarized in Tab. 1. For results by ZE, the growth rate $G = \text{Im}\sigma$ is directly calculated by Eq. (8). The dimensionless growth rate is defined as $G' = \text{Im}(\sigma)/\frac{1}{2}\omega_0 k_0^2 a_0^2$. For results by HOS method, the growth rate is estimated by data fitting using a least-squares method. The average amplitude of the upper and lower sideband, which is normalized by the initial amplitude of the carrier wave, is used for calculation. The length of the data is about $50T_1$. For example, the slope of $50T_1$ to $100T_1$ in Fig. 2 is considered as the growth rate. It is found that the results by the HOS method are in good agreement with those by ZE for all the cases. The maximum growth rate decreases with decreasing depth, which indicates the reduction of the modulational instability. The most unstable mode occurs only in deep water when the sidebands are collinear with the carrier wave, whereas in finite depth the region with an angle around 35° exhibits the strongest modulational instability.

In Fig. 2, analyses in wavenumber space are performed and the amplitudes of two sidebands (the magenta solid line for $\boldsymbol{k_3}$, the blue solid line for $\boldsymbol{k_4}$ and the black dash dot line for the average) and the carrier wave (the black solid line) are plotted at each time step. The prediction of ZE is also plotted as the black dash line for comparison. It can be seen from the figure that the amplitudes of the sidebands increase rapidly while the amplitude of the carrier wave decreases. The slopes of the sidebands by ZE and the HOS method are almost the same. The steady growth time of the sidebands (the straight line segments for the sidebands in Fig. 2) increases with decreasing the depth. However, there is no significant difference for the maximum values that the sidebands can reach (the first peak of the sideband growth curve) in different depths.

When modulation occurs, the energy of the carrier wave is transferred to the upper and lower sidebands.

Table 1: Cases of the numerical simulations.

Case	k_0h	k_0a_0	K_x/k_0	K_y/k_0	G		G'	
					ZE	HOS	ZE	HOS
A1	100	0.10	0.18	0	0.0126	0.0127	0.8059	0.8078
B1	1.78	0.10	0.24	0.18	0.0094	0.0096	0.6198	0.6295
C1	1.363	0.10	0.24	0.18	0.0085	0.0086	0.5783	0.5883
D1	1.24	0.10	0.22	0.16	0.0079	0.0080	0.5497	0.5543
E1	1.0	0.10	0.26	0.18	0.0065	0.0066	0.4741	0.4805
F1	0.8	0.10	0.36	0.22	0.0051	0.0051	0.3998	0.4003

The amplitudes of two sidebands increase exponentially in the wavenumber space. In the real physical space, the maximum free-surface elevation will increase with the time. The amplification of the wave amplitude is also an appropriate criterion for assessing the modulational instability. Fig. 3 illustrates the temporal evolution of the maximum wave elevation which is normalized by the initial amplitude of the carrier wave. The continuous increase gives another evidence for the modulational instability. In addition, for deep water, the maximum wave elevation can reach a relatively higher value in less time than that for the shallower water.
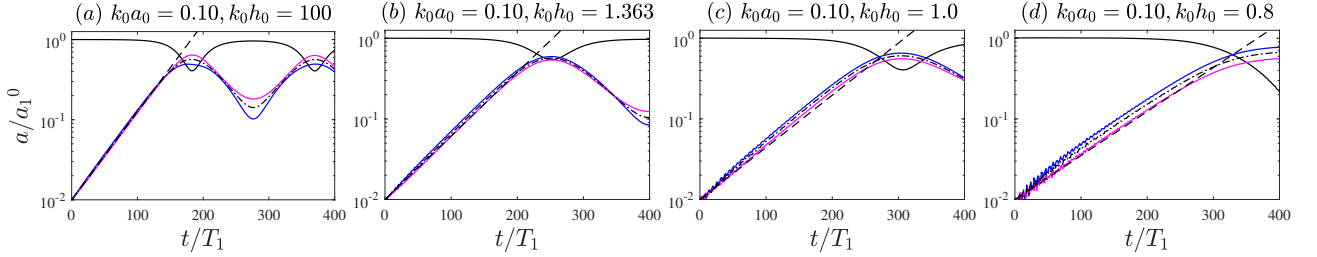
Figure 2: Temporal evolution of the amplitudes of the carrier wave and sidebands in several different depths.
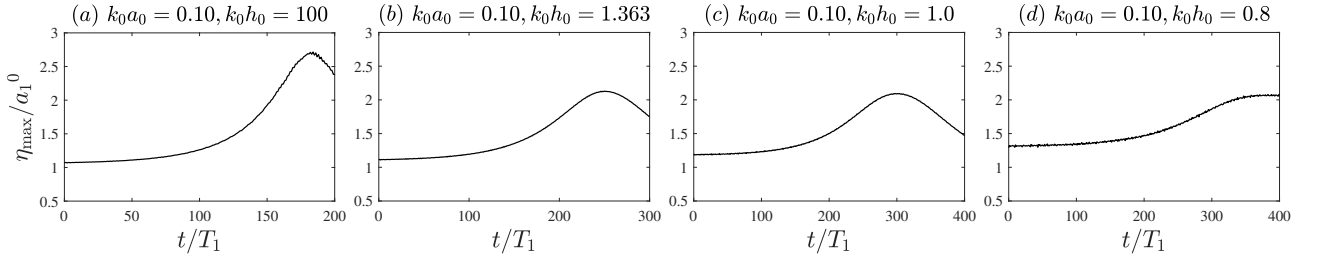
Figure 3: Temporal evolution of the normalised maximum elevation of the free surface in several different depths.

References

BENJAMIN, T. B. 1967 Instability of periodic wavetrains in nonlinear dispersive systems. *Proc. R. Soc. Lond. A* **299** (1456), 59–76.

BENNEY, D. J. & ROSKES, G. J. 1969 Wave instabilities. *Stud. Appl. Math.* **48** (4), 377–385.

CRAWFORD, D. R., LAKE, B. M., SAFFMAN, P. G. & YUEN, H. C. 1981 Stability of weakly nonlinear deep-water waves in two and three dimensions. *J. Fluid Mech.* **105** (-1), 177–191.

DOMMERMUTH, D. & YUE, D. K. P. 1987 A higher-order spectral method for the study of nonlinear gravity waves. *J. Fluid Mech.* **187**, 267–288.

FERNANDEZ, L., ONORATO, M., MONBALIU, J. & TOFFOLI, A. 2014 Modulational instability and wave amplification in finite water depth. *Nat. Hazard. Earth Sys.* **14** (3), 705–711.

GRAMSTAD, O. & TRULSEN, K. 2011 Hamiltonian form of the modified nonlinear schrödinger equation for gravity waves on arbitrary depth. *J. Fluid Mech.* **670**, 404–426.

JANSSEN, P. A. E. M. 2009 On some consequences of the canonical transformation in the hamiltonian theory of water waves. *J. Fluid Mech.* **637**, 1–44.

JANSSEN, P. A. E. M. & ONORATO, M. 2007 The intermediate water depth limit of the zakharov equation and consequences for wave prediction. *J. Phys. Oceanogr.* **37**, 2389–2400.

LIU, S. & ZHANG, X. 2019 Extreme wave crest distribution by direct numerical simulations of long-crested nonlinear wave fields. *Appl. Ocean Res.* **86**, 141–153.

MCLEAN, J. W. 1982 Instabilities of finite-amplitude gravity waves on water of finite depth. *J. Fluid Mech.* **114**, 331–341.

MEI, C. C., STIASSNIE, M. & YUE, D. K. P. 2005 *Theory and Applications of Ocean Surface Waves, Part 2: Nonlinear Aspects.* World Scientific.

STIASSNIE, M. & GRAMSTAD, O. 2009 On Zakharov's kernel and the interaction of non-collinear wavetrains in finite water depth. *J. Fluid Mech.* **639** (639), 433–442.

STIASSNIE, M. & SHEMER, L. 1984 On modifications of the zakharov equation for surface gravity waves. *J. Fluid Mech.* **143**, 47–67.

TOFFOLI, A., FERNANDEZ, L., MONBALIU, J., BENOIT, M., GAGNAIRE-RENOU, E., LEFEVRE, J. M., CAVALERI, L., PROMENT, D., PAKOZDI, C., STANSBERG, C. T., WASEDA, T. & ONORATO, M 2013 Experimental evidence of the modulation of a plane wave to oblique perturbations and generation of rogue waves in finite water depth. *Phys. Fluids* **25** (9), 091701.

WEST, B. J., BRUECKNER, K. A. & JANDA, R. S. 1987 A new numerical method for surface hydrodynamics. *J. Geophys. Res.* **92** (11), 11803–11824.

WHITHAM, G. B. 1967 Non-linear dispersion of water waves. *J. Fluid Mech.* **27** (2), 399–412.

ZAKHAROV, V. E. 1968 Stability of periodic waves of finite amplitude on the surface of a deep fluid. *J. Appl. Mech. Tech. Phys.* **9** (2), 190–194.

ZAKHAROV, V. E. 1999 Statistical theory of gravity and capillary waves on the surface of a finite-depth fluid. *Eur. J. Mech. B* **18** (3), 327–344.